



Fabrication of P25/Ag₃PO₄/graphene oxide heterostructures for enhanced solar photocatalytic degradation of organic pollutants and bacteria

Xiaofei Yang*, Jieling Qin, Yan Jiang, Kangmin Chen, Xuehua Yan, Du Zhang, Rong Li, Hua Tang

School of Materials Science and Engineering, Jiangsu University, Zhenjiang 212013, China

ARTICLE INFO

Article history:

Received 15 September 2014

Received in revised form

12 November 2014

Accepted 15 November 2014

Available online 21 November 2014

Keywords:

Ag₃PO₄

Graphene oxide

Composite materials

Photocatalytic

Bactericidal

ABSTRACT

Herein we demonstrate a facile and general process for fabricating P25/silver orthophosphate/graphene oxide (P25/Ag₃PO₄/GO) ternary composite materials using electrostatically-driven assembly and ion-exchange method. The composite materials reveal a well-defined heterostructure where few-layer GO sheets are decorated with micro-sized Ag₃PO₄ particles and TiO₂ nanoparticles. The photodegradation of dye molecule and inactivation of bacteria can be tuned by varying the added amount of GO and the molar ratio of Ag₃PO₄/P25. The photocatalytic activity for degrading organic dye molecule and bactericidal performance could be improved by synergistic effects derived from the P25/Ag₃PO₄/GO heterostructure. A detailed analysis of the reactions mechanism by radical-capture agents suggests photo-induced active holes and reactive oxygen species (ROS) are responsible for the enhanced photocatalytic degradation activity owing to effective visible light harvesting, improved separation efficiency and fast interfacial charge transfer. Intrinsic antibacterial activity of dissolved Ag⁺ ions is also considered to play an important role in determining the excellent bactericidal performance of the P25/Ag₃PO₄/GO ternary composite. We believe that this work provides new insights into the low-cost, large-scale production of multifunctional composite materials for the applications in solar photocatalytic degradation of harmful volatile organic compounds (VOCs) and common pathogenic bacteria in wastewater.

© 2014 Elsevier B.V. All rights reserved.

1. Introduction

Water pollution has become a global issue of concern over the past few decades and it continues to threaten both quality of life and public health in the world. The composition of wastewater is varied and can include toxic chemicals, bacteria and viruses, although various strategies have been explored for [1–6], it still remains a great challenge to eliminate harmful chemicals, particularly volatile organic compounds (VOCs), and disease-causing microorganisms simultaneously using a single material. One means of achieving this objective would be implementation of new bifunctional composite materials capable of efficiently degrading organic pollutants and eliminating common pathogenic bacteria via an eco-friendly process.

Semiconductors have been proved to be a promising material as photocatalysts for decontamination and purification of wastewater [7–13]. The most attractive feature is that reactive oxygen species (ROS) and active holes produced in the irradiated semiconductor-based photocatalytic system allow the destruction of a wide range of organic pollutants and bacteria. One of the most studied photocatalyst is TiO₂. The use of different TiO₂ nanostructures has been extensively investigated in the photodegradation of organic pollutants [14–21]. However, due to its wide band gap, TiO₂ can only be excited by UV light (less than 400 nm). Thus the construction of TiO₂-based composite materials with improved lower band gap is crucial for the increase of the solar energy harvest. Most recently, silver orthophosphate (Ag₃PO₄) has attracted increasing attention owing to its great potential in water splitting and photodegradation of organic pollutants [22–29]. However, Ag₃PO₄ suffer from poor photostability due to fast photoreduction into metallic Ag. Thus many efforts were made to overcome the above disadvantages and a variety of Ag₃PO₄-based composite photocatalysts were suggested [30–36]. Graphene oxide (GO) is considered to be one of the most promising layer materials for

* Corresponding author. Tel.: +86 511 88790191; fax: +86 511 88791947.

E-mail addresses: xyang@mail.ujs.edu.cn (X. Yang), tanghua@mail.ujs.edu.cn (H. Tang).

Table 1
Reaction conditions for the preparation of hydrothermal products.

Sample	GO	AgNO ₃	P25	Na ₂ HPO ₄ ·7H ₂ O	M (Ag ₃ PO ₄ /P25)
M-0	20 mg	9 mmol, 1.53 g		3 mmol, 0.8 g	
M-1	20 mg	9 mmol, 1.53 g	3 mmol, 0.24 g	3 mmol, 0.8 g	1
M-0.8	20 mg	9 mmol, 1.53 g	3.75 mmol, 0.3 g	3 mmol, 0.8 g	0.8
M-0.6	20 mg	9 mmol, 1.53 g	5 mmol, 0.4 g	3 mmol, 0.8 g	0.6
M-0.4	20 mg	9 mmol, 1.53 g	7.5 mmol, 0.6 g	3 mmol, 0.8 g	0.4
M-0.2	20 mg	9 mmol, 1.53 g	15 mmol, 1.2 g	3 mmol, 0.8 g	0.2
GO-0		9 mmol, 1.53 g	3.75 mmol, 0.3 g	3 mmol, 0.8 g	0.6
GO-10	10 mg	9 mmol, 1.53 g	3.75 mmol, 0.3 g	3 mmol, 0.8 g	0.6
GO-20	20 mg	9 mmol, 1.53 g	3.75 mmol, 0.3 g	3 mmol, 0.8 g	0.6
GO-50	50 mg	9 mmol, 1.53 g	3.75 mmol, 0.3 g	3 mmol, 0.8 g	0.6
GO-100	100 mg	9 mmol, 1.53 g	3.75 mmol, 0.3 g	3 mmol, 0.8 g	0.6
GO-200	200 mg	9 mmol, 1.53 g	3.75 mmol, 0.3 g	3 mmol, 0.8 g	0.6

the construction of functional composite materials [37–40]. The availability of oxygen-containing functional groups on the surface allows GO to interact with inorganic and organic so that a wide range of functional composites with unusual properties can be readily synthesized. Furthermore, its high surface area favors the deposition of different functional components on the surface and helps increase the adsorption capacity of chemicals and bacteria. Although several kinds of TiO₂-based and Ag₃PO₄-based composite materials have been synthesized [41–49], to the best of our knowledge, the design and facile synthesis of bifunctional Ag₃PO₄-based ternary composite materials is scarce.

Herein, we present the fabrication and characterization of P25/Ag₃PO₄/GO ternary composites as photocatalyst for the degradation of rhodamine B (RhB) dye molecules and the inactivation of bacteria. The ternary heterostructure allow better visible light harvesting, short diffuse distance for charge transport and a large contact area for fast interfacial charge separation and photochemical reactions. The photocatalytic activity and stability of composites were investigated, and bactericidal performance of the obtained samples was also evaluated by minimum inhibitory concentrations (MIC), minimum bactericidal concentrations (MBC) and time-kill study.

2. Experimental

2.1. Synthesis of samples

All reagents was purchased from Sinopharm Chemical Reagent Co. Ltd. (Shanghai, China) and used as received without further purification. Graphite oxide was synthesized from natural graphite by a modified Hummers' method with additional KMnO₄ [50]. In a typical synthesis, the obtained graphite oxide was ultrasonicated in distilled water for 2 h to give GO dispersions. AgNO₃ aqueous solution was then added dropwise into GO dispersions under magnetic stirring. After gently stirring overnight, Degussa P25 aqueous dispersions was added slowly into the Ag⁺/GO mixture, the mixed

solution was stirred for further 30 min, followed by the addition of Na₂HPO₄ aqueous solution into the P25/Ag⁺/GO mixture. Upon the addition of Na₂HPO₄, yellowish-brown precipitates were formed instantaneously. The obtained product was collected by centrifugation, washed several times with deionized water and absolute ethanol, and dried at 60 °C in vacuum overnight. The reaction conditions for the preparation of composites are shown in Table 1 and the overall synthetic procedure for the generation of P25/Ag₃PO₄/GO composites is illustrated in Fig. 1. The P25/Ag₃PO₄/GO composites with different amounts of GO are denoted as GO–X (X is the actual mass of GO used, in mg), while the composites with different molar ratios of Ag₃PO₄/TiO₂ are denoted as M–X (X is the calculated molar ratio of Ag₃PO₄/P25 where the amounts of Ag₃PO₄ and GO are fixed, X-0 represents the Ag₃PO₄/GO composite).

2.2. Characterization

The morphologies of the as-synthesized products were examined by field-emission scanning electron microscopy (FE-SEM, JEOL, JSM-7001F), transmission electron microscopy (TEM, JEOL, JEM-2100). The phases of the obtained products were collected on a Bruker D8 Advance X-ray diffractometer (Cu K α radiation, $\lambda = 0.15406$ Å) in a 2θ range from 10° to 80° at room temperature. Raman experiments were performed using a DXR spectrometer using the 532 nm laser line and measurements were made in backscattering geometry. The light harvesting ability was evaluated by using UV–vis diffuse reflectance spectroscopy within 200–800 nm wavelength range using a Shimadzu UV2450 spectrometer. The surface electronic states were analyzed by using X-ray photoelectron spectroscopy (XPS, Perkin–Elmer PHI 5000 C).

2.3. Photocatalytic experiments

The photocatalytic activities of products were valued by the decomposition of organic dye rhodamine B (RhB) under visible-light irradiation. The optical system for the photocatalytic reaction

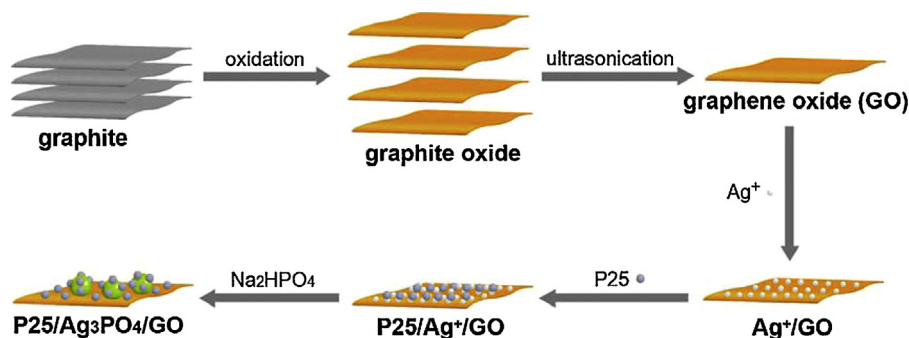


Fig. 1. Schematic illustrating the preparation of P25/Ag₃PO₄/GO composites.

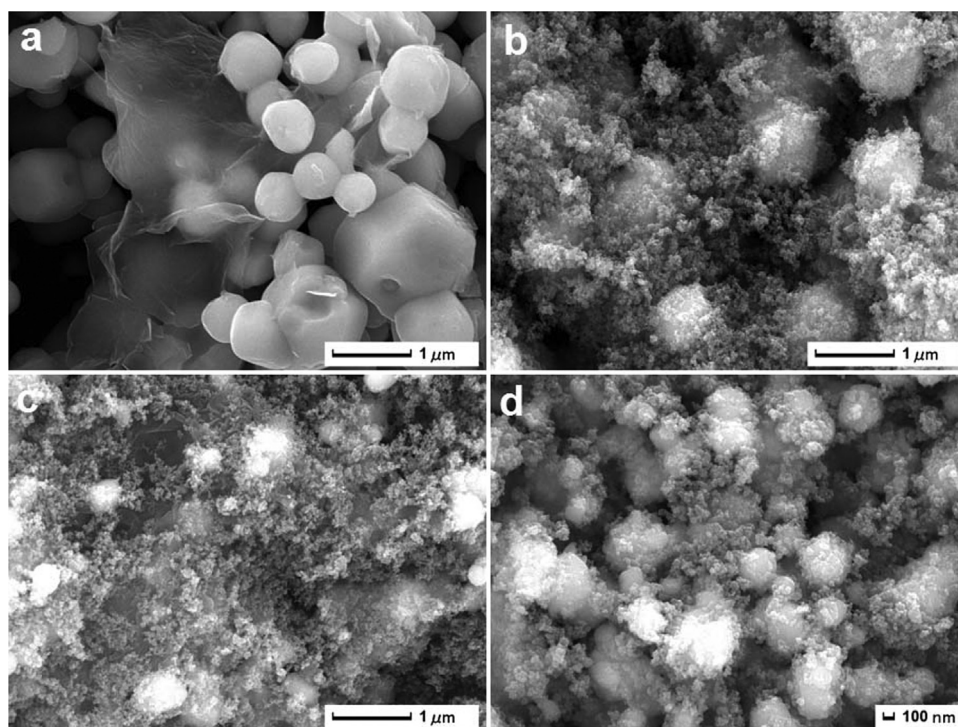


Fig. 2. FE-SEM images of the Ag₃PO₄/GO composite M-0 (a), the P25/Ag₃PO₄ composite GO-0 (b), and the P25/Ag₃PO₄/GO composite M-0.6 (c and d).

was composed of a 350 W Xe lamp and a cut-off filter ($\lambda > 420$ nm). RhB solutions (100 mL, 10^{-5} mol/L) containing 50 mg of samples were put in a sealed glass beaker and first ultrasonicated, and then stirred in the dark to ensure absorption–desorption equilibrium. After visible light illumination, 3 mL of samples were taken out at regular time intervals and separated through centrifugation. The supernatants were analyzed by recording variations of the absorption band maximum in the UV–vis spectra of the dye molecule by using a Lambda 25 UV/vis spectrophotometer.

2.4. Evaluation on antibacterial activities of samples

Bacteria was cultivated in nutrient broth at 37 °C for 18 h in a rotary shaker until reaching stationary growth phase. The as-prepared cells were then resuspended and diluted to the required cell density of around 10^7 colony-forming units per milliliter (CFU/mL) with sterilized saline solution (0.9% NaCl). The antibacterial activity of the composites was tested on six bacterial strains *Escherichia coli*, *Staphylococcus aureus*, *Salmonella typhi*, *Pseudomonas aeruginosa*, *Bacillus subtilis*, *Bacillus pumilus* from ATCC. All of the bactericidal experiments were performed at room temperature and repeated three times in order to give an average value; the measured data for each set of experiments were expressed with the mean and standard deviation.

The minimum inhibitory concentrations (MIC) of each of composites were determined against all test strains. Various concentrations (6.25 ppm, 12.5 ppm, 25 ppm, 50 ppm, 100 ppm, 200 ppm) of the composites were mixed with freshly sterilized (121 °C, 15 min) and nutrient broth (tempered at 37 °C) in glass tubes (15 mm × 15 mm), consequently 100 μL of pre-cultured strain (initial concentration 10^6 CFU/mL) was added into each tube by micropipette. All the tubes were then placed in a precision constant temperature incubator at 35 °C for 48 h where a high-pressure mercury lamp (Philips HPR 125 W) was used as light source. MIC was determined as the lowest composite concentration that resulted in complete inhibition in nutrient broth. For the minimum bactericidal concentration (MBC), the mixtures of a series

of concentrations (MIC, 2MIC, 4MIC, ...) of composite dispersions with test strains were drawn with one loop full streak-inoculated to the nutrient agar plates, respectively. All the plates were then placed in the same incubator equipped with the same light source at 35 °C for 48 h. MBC was determined as the lowest composite concentration that appeared without any colonies could be observed on the plates.

In order to further investigate the effect of the antibacterial composite on the bacteria cells, the best sample M-0.6 was chosen as the best antibacterial composite from the MIC and MBC results and the colonies were counted to determine the viable bacterial numbers after being incubated. In a typical process, PBS buffer was first prepared from a mixture of 0.2 M NaH₂PO₄ and 0.2 M Na₂HPO₄ aqueous solutions, M-0.6 dispersion with the concentration of 200 ppm was then mixed with sterilized PBS solution, followed by the addition of pre-cultured strain to reach the cell concentration of 10^6 CFU/mL. All the tubes were then incubated in a temperature-controlled rotary shaker at 20 °C for different times (0, 0.5 h, 1 h, 2 h, 4 h). For TEM characterizations of untreated and treated samples, 10 μL of each specimen dispersion was loaded on TEM copper grids and was then stained with tungstophosphoric acid aqueous solution. The air-dried copper grids were examined using the TEM (JEOL JEM-2100).

3. Results and discussion

Morphological features of different samples were examined by field emission scanning electron microscopy (FE-SEM) and the corresponding images are shown in Fig. 2. Fig. 2a shows FE-SEM images of the resulting Ag₃PO₄/graphene oxide composite in the absence of P25, in which curved graphene oxide sheets are decorated with irregular Ag₃PO₄ particles. While for the Ag₃PO₄/P25 composite, the surfaces of Ag₃PO₄ particles are covered by randomly distributed TiO₂ nanoparticles. As shown in Fig. 2c, when graphene oxide was introduced into the Ag₃PO₄/P25 composite, it can act as the support for both Ag₃PO₄ and TiO₂ particles, the size of Ag₃PO₄ particles in the Ag₃PO₄/P25/GO composite is smaller compared to

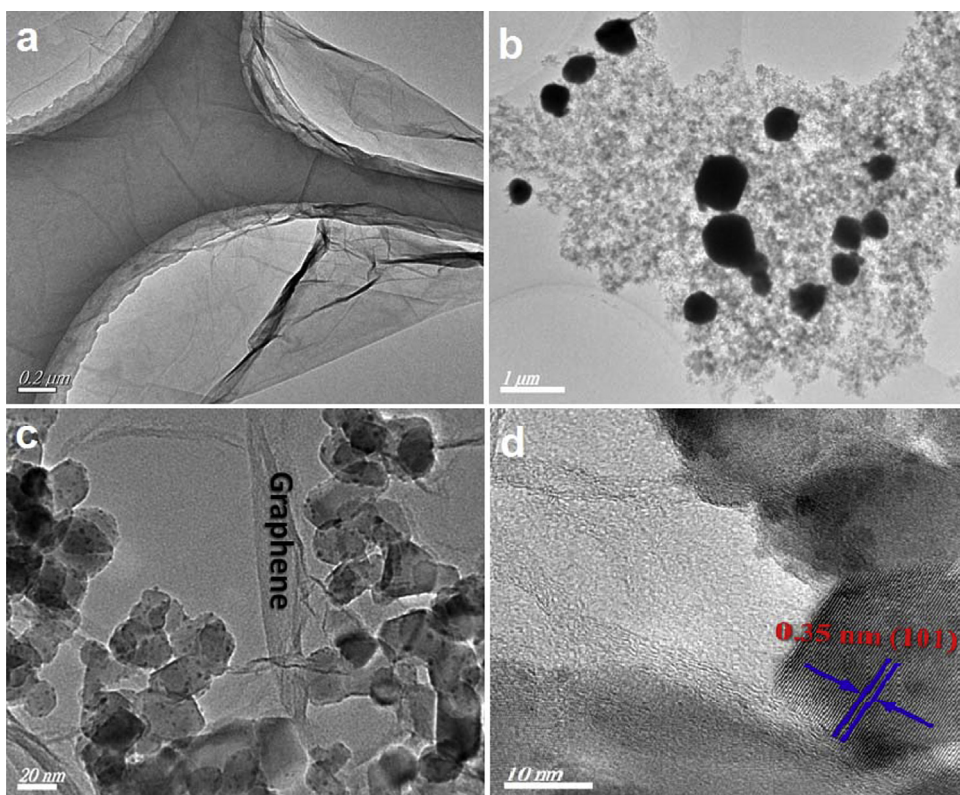


Fig. 3. TEM image of GO (a), low-magnification (b), high-magnification (c) TEM images and HRTEM image (d) of the P25/Ag₃PO₄/GO composite M-0.6.

one in the Ag₃PO₄/P25 composite, suggesting that the negatively-charged graphene oxide plays an important role in the nucleation and controlled growth Ag₃PO₄ by electrostatically-driven interactions. The enlarged FE-SEM image of the Ag₃PO₄/P25/GO composite shown in Fig. 2d further reveals the hybridization of TiO₂ nanoparticles with Ag₃PO₄ and graphene oxide.

Further information about the morphological characteristic of different components in the composite was obtained from transmission electron microscopy (TEM) and high-resolution TEM images. TEM image shown in Fig. 3a verifies the typical wrinkled, high surface area and ultrathin nanosheet morphology of graphene oxide. Fig. 3b and c shows the micro-/nanostructure of the three-phase P25/Ag₃PO₄/GO composite. It is clearly shown that micro-sized Ag₃PO₄ particles (0.3–0.7 μm) and TiO₂ nanoparticles grow on the surface of graphene oxide. The presence of nano-sized TiO₂ and few-layer GO nanosheets was further confirmed by enlarged TEM image (Fig. 3c) of the P25/Ag₃PO₄/GO composite on selected area. GO nanosheets decorated with TiO₂ nanoparticles with an average diameter of 25 nm were observed. The subsequent HRTEM image shown in Fig. 3d reveals that the nanostructured TiO₂ is wrapped by few layers of GO. Furthermore, the fringes of individual TiO₂ nanoparticles with a lattice spacing of 0.35 nm can be assigned to the (1 0 1) plane of anatase TiO₂.

It has been reported that the use of GO as the precursor for composite photocatalysts can effectively tailor the size and shape of additional semiconductor due to the electrostatic interaction. Thus in order to evaluate the effect of GO amount on the morphology of Ag₃PO₄ particles in the composites, FE-SEM images of P25/Ag₃PO₄/GO composites with different amounts of GO were recorded and are shown in Fig. 4. When GO is absence, the aggregates of micro-sized Ag₃PO₄ and TiO₂ nanoparticles were observed in Fig. 4a. The introduction of 10 mg GO resulted in the formation of more dense composites where GO sheets are considered as the support for Ag₃PO₄ and TiO₂ particles. Further increase in the GO

amount from 10 mg to 20 mg led to the generation of Ag₃PO₄ particles with smaller sizes. However, the use of more than 20 mg GO (50 mg, 100 mg) as the precursor caused the increase in the diameters of Ag₃PO₄ particles, and the presence of 200 mg GO in the composite demonstrates that the majority of Ag₃PO₄ and TiO₂ particles are coated or wrapped by GO sheets.

The P25/Ag₃PO₄/GO composites were further characterized by powder X-ray diffraction (XRD) and Raman spectroscopy. As shown in Fig. 5a, the majority of the diffraction peaks can be readily indexed to Ag₃PO₄ (JCPDS 06-0505, body-centered cubic) and the rest match those of the crystalline anatase TiO₂ (JCPDS 21-1272). Due to the high crystallinity of TiO₂ and Ag₃PO₄, no peaks from GO were observed. However, the presence of GO in the composite can be discerned by Raman spectroscopy (Fig. 5b). The typical Raman spectrum of GO exhibits two peaks at 1350 and 1590 cm⁻¹, corresponding with the well-documented D (k-point phonons of A_{1g} symmetry) and G peaks (E_{2g} phonon of sp² carbons), respectively. The Raman spectrum for the P25/Ag₃PO₄ composite shows several characteristic peaks ranging from 50–1200 cm⁻¹, corresponding to the E_g, A_{1g} and B_{1g} modes of anatase TiO₂. The typical peaks from Ag₃PO₄ (in the range of 500–1300 cm⁻¹) could not distinguish due to the overlapping from peaks from both two materials. Notably, both two peaks (D peak and G peak) for the graphitized structures and characteristic peaks from Ag₃PO₄ and TiO₂ were observed in the P25/Ag₃PO₄/GO composite S0.6, confirming the hybridization of graphene oxide and two semiconductors. Also the observed intensity ratio I_D/I_G (0.9) in the composite is close to that (0.91) of GO, indicating the similarity of GO structure in the P25/Ag₃PO₄/GO composite.

The incorporation of GO into the Ag₃PO₄/P25 composite leads to the enhancement in light absorption over the entire visible light region of 400–800 nm (Fig. 6a). When the added GO amount was fixed to 20 mg, the decrease of molar ratio (mAg₃PO₄/P25) from 1 to 0.6 witnesses significant enhancement in light absorption intensity

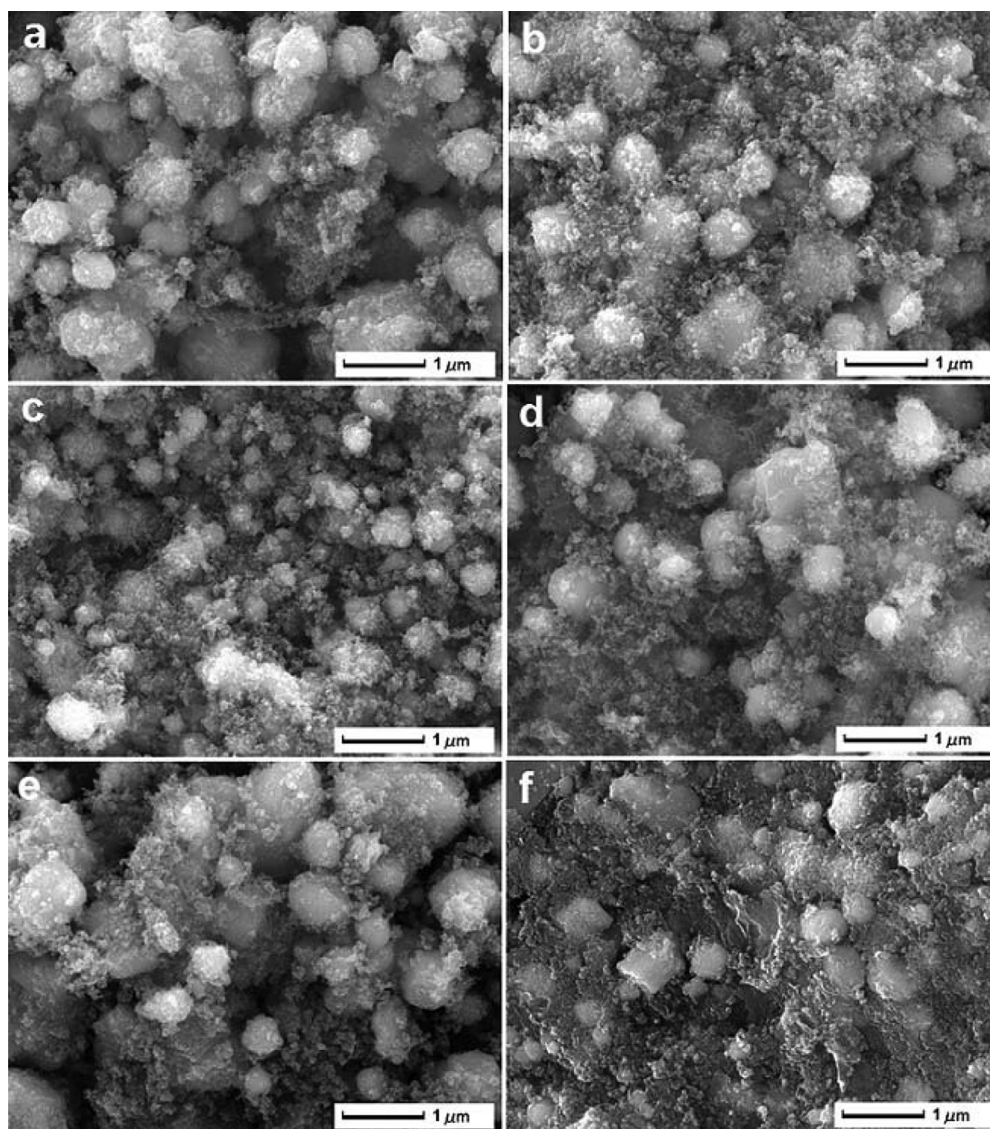


Fig. 4. FE-SEM images of the composites GO-0 (a) and GO-10 (b), GO-20 (c), GO-50 (d), GO-100 (e) and GO-200 (f).

(Fig. 6b). However, the composites with lower molar ratios than 0.6 (0.4, 0.2 and 0.1), where more P25 were employed, exhibit weaker light absorption ability in comparison with the composite with a molar ratio of 0.6. The results imply that the P25/Ag₃PO₄/GO composite M-0.6 may be able to utilize more visible light to generate photo-induced electron-hole pairs and thus demonstrate improved solar photocatalytic activity.

Furthermore, X-ray photoelectron spectroscopy (XPS) measurement was performed to determine quantitative information related to the chemical state, type, composition and the nature of functional groups involved in the P25/Ag₃PO₄/GO composite. Fig. 7a shows the XPS survey spectrum of the three-phase composite where the presence of carbon, oxygen, silver, titanium and phosphorus is revealed, no other elemental contaminants were detected. The peak at 284.8 eV in the high-resolution C 1s spectrum shown in Fig. 7b is attributed to sp² hybridized non-oxygenated ring carbon atoms (C–C), while the other peaks at 286.8 eV and 288.7 eV assigned to the oxygen-containing epoxy/hydroxyl groups (C–O) and carbonyls (C=O), respectively. The presence of oxygen-containing functional groups accounts for more than 60% of total carbon while less than 40% graphitic carbon exists in the composite, indicating the internal consistency of GO structure in

the composite. Moreover, phenomena of spin orbit separation, 6.0 eV between Ag 3d_{5/2} (367.7 eV) and Ag 3d_{3/2} (373.8 eV) peaks in Fig. 7c, as well as between Ti 2p_{3/2} (458.8 eV) and Ti 2p_{1/2} (464. eV) in Fig. 7d, suggest the existence of Ag⁺ and Ti⁴⁺ in the composite.

The removal efficiency of the pollutant was studied by the adsorption and visible-light-driven photocatalytic degradation of the dye molecule RhB as a model system. It is clearly shown in Fig. 8a that, without GO, the two-phase P25/Ag₃PO₄ composite revealed around 5% adsorption toward RhB in dark and showed an degradation efficiency of 53% in 1 h under illumination. With the increasing amount of GO, an obvious enhancement in the dye adsorption was observed for all photocatalysts. However, the presence of GO in the composite favored the improved photocatalytic activity when the amount was increased from 0 to 20 mg. The use of more than 20 mg GO (i.e. 50 mg) in the composite led to a gradual decrease in the degradation activity from ~80% to less than ~50% in 1 h, in addition, the use of more GO such as 100 and 200 mg in the composite further weakened the photocatalytic performance to 30% and 25%, respectively. The phenomena imply that the addition of a proper amount of GO has a remarkable effect on the adsorption and photocatalytic performance of the composite. It is well-known that high-surface-area GO sheets

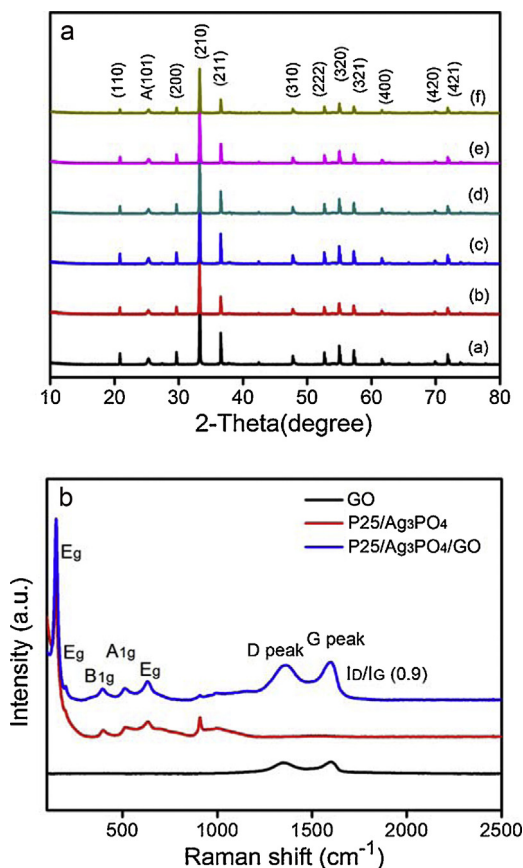


Fig. 5. (a) XRD spectra of composite materials prepared from different amounts of GO (a: GO-0, b: GO-10, c: GO-20, d: GO-50, e: GO-100, f: GO-200); (b) Raman spectra of GO, P25/Ag₃PO₄ and the P25/Ag₃PO₄/GO composite.

favor the dye adsorption and may promote the improved photocatalytic activity, nevertheless the presence of excess amounts of GO in the composite could also cover the active surfaces or sites of Ag₃PO₄, leading to obvious decrease in visible light photocatalytic performance of the composite. Thus the optimal amount of GO in the P25/Ag₃PO₄/GO composite is 20 mg. Consequently, when the GO amount involved in the composite was fixed, the photocatalytic degradation performance of RhB over different composite with different molar ratios of Ag₃PO₄/P25 was also investigated and results are shown in Fig. 8b. When P25 was absent, the Ag₃PO₄/GO composite M-0 exhibited a degradation efficiency of around 50% in 1 h, however, the efficiency was gradually enhanced to 55% and 75% with decreasing molar ratios of 0.8 and 0.6, respectively. The introduction of more P25 (M-0.4 and M-0.2) into the composite caused even worse efficiencies than the Ag₃PO₄/GO composite (M-0). The overall results demonstrate that both the GO amount and the molar ratio of Ag₃PO₄/P25 play crucial roles in determining visible-light-driven photocatalytic performance of the composites.

In order to reveal the active radicals responsible for the enhanced photocatalytic activity, three different chemicals p-benzoquinone (BZQ, an O₂^{•−} radical scavenger), disodium ethyl-enediaminetetraacetic acid (Na₂-EDTA, a hole scavenger) and *tert*-butanol (an •OH radical scavenger) were employed as scavengers for holes and radicals trapping experiments. As shown in Fig. 8c, when 5 mM Na₂-EDTA was added, a notable inhibitory effect on the degradation activity over the P25/Ag₃PO₄/GO composite (M-0.6) was observed, in which less than 10% RhB was degraded. The presence of 5 mM *tert*-butanol in the photocatalytic system showed a negligible effect on the degradation of RhB where almost 95% RhB was degraded. The addition of 5 mM BZQ caused similar effect on

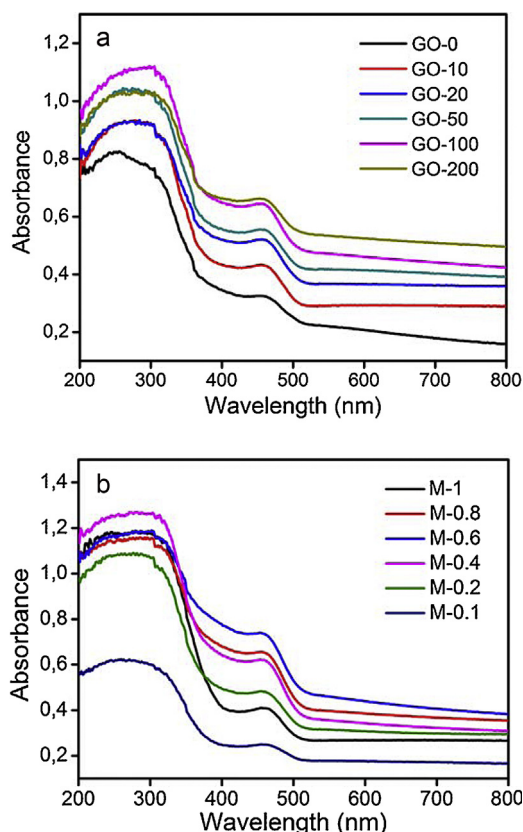


Fig. 6. UV-vis diffuse reflectance spectra of composites prepared in the presence of different amounts of GO (a) and different molar ratios of Ag₃PO₄/P25.

the RhB degradation, in which only 15% was degraded. It is suggested from holes and radicals trapping experiments that active photoinduced holes and O₂^{•−} radicals, rather than •OH radicals, are dominant species responsible for its highly efficient photocatalytic activity. The stability of the composite (M-0.6) was further evaluated by collecting the used sample after photocatalysis and performing the repeated experiments of the photocatalyst under similar conditions. It is clearly shown in Fig. 8d that, after 5 repeated experiments, a photocatalytic degradation efficiency of more than 80% was achieved, indicating that the obtained composite (M-0.6) demonstrates a good recyclability.

It has been proven that microbial cells could be killed by irradiated TiO₂ photocatalyst, and TiO₂ has demonstrated a wide variety of applications in water purification, sterilization of food. Furthermore, silver's association with antibacterial properties has long been established, silver is not toxic for humans and the antibacterial action of silver is dependent on the silver ion. Thus for the purpose of obtaining bifunctional for practical applications, the inactivation of microorganisms and bacterial killing over different irradiated composite photocatalysts have been evaluated initially by the minimum inhibitory concentration (MIC) and minimum bactericidal concentration (MBC), the MIC and MBC results are shown in Table 2. It is notable that all composites demonstrated excellent bacterial inhibition activities against four different pathogenic bacteria, MIC values lower than 100 ppm were obtained against *S. aureus*, *S. typhi* and *P. aeruginosa* for the majority of composite materials under light irradiation. The bactericidal activities of all irradiated samples were further confirmed by MBC results where most of the observed MBC values are lower than 200 ppm. For the composites obtained from different amounts of GO, it is clearly shown that both MIC and MBC values decreased with the increasing GO amounts from 0 to 20 mg, however the presence of more than

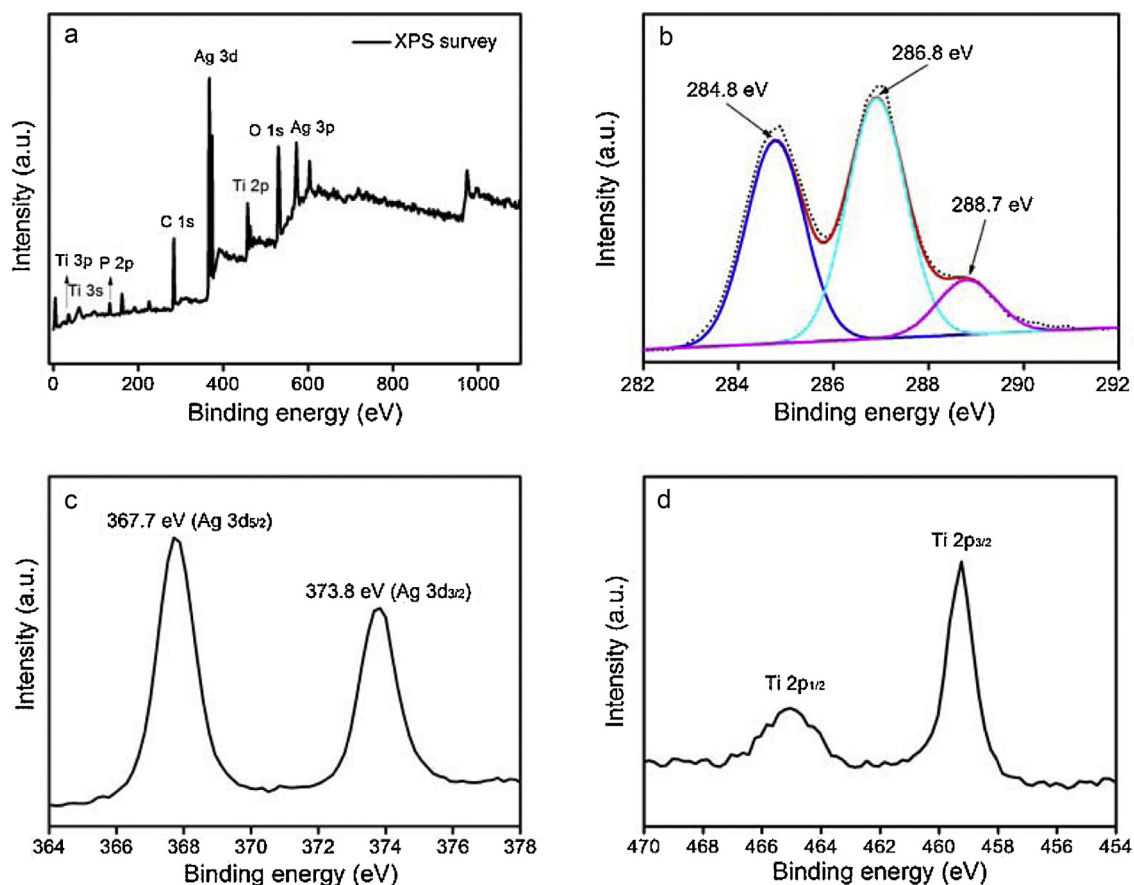


Fig. 7. XPS profile (a); curve fit of the high-resolution C 1s peak (b); the high-resolution Ag 3d peak (c) and Ti 2p peak (d) of the composite M-0.6.

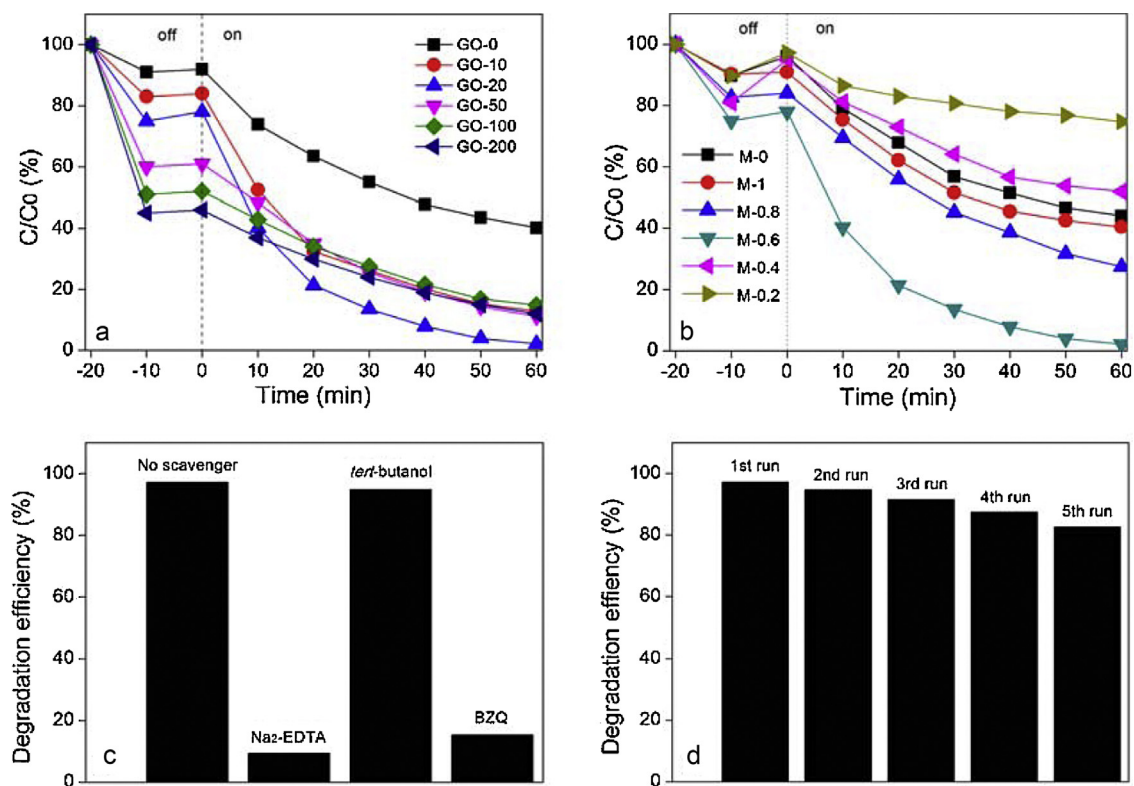


Fig. 8. Dye removal efficiency over photocatalysts with different GO amounts (a); with different molar ratios of $\text{Ag}_3\text{PO}_4/\text{P25}$ (b); holes and radicals trapping experiments (c); recycled photodegradation (d) of the composite M-0.6.

Table 2
MIC and MBC results of the obtained composite materials.

Sample	MIC (MBC)			
	<i>E. coli</i>	<i>S. aureus</i>	<i>S. typhi</i>	<i>P. aeruginosa</i>
GO-0	100 (100)	50 (100)	50 (100)	50 (50)
GO-10	100 (100)	25 (50)	25 (25)	25 (25)
GO-20	100 (100)	12.5 (25)	12.5 (12.5)	12.5 (25)
GO-50	100 (100)	50 (50)	50 (100)	50 (50)
GO-100	100 (100)	50 (100)	100 (100)	50 (100)
GO-200	100 (100)	100 (200)	200 (200)	100 (200)
M-0	100 (100)	50 (100)	6.25 (12.5)	12.5 (50)
M-1	100 (100)	25 (50)	6.25 (12.5)	12.5 (50)
M-0.8	100 (100)	12.5 (25)	6.25 (12.5)	6.25 (12.5)
M-0.6	100 (100)	6.25 (12.5)	6.25 (6.25)	6.25 (6.25)
M-0.4	100 (100)	100 (200)	12.5 (25)	25 (100)
M-0.2	100 (100)	100 (400)	12.5 (50)	50 (200)

Bold indicates the best one out of six samples compared with others.

Table 3
MIC and MBC results of different materials under different conditions.

Sample	MIC (MBC)			
	<i>E. coli</i>	<i>S. aureus</i>	<i>S. typhi</i>	<i>P. aeruginosa</i>
Ag ₃ PO ₄ + light	200 (400)	100 (200)	200 (200)	200 (400)
P25 + light	200 (200)	50 (100)	50 (50)	50 (50)
M-0.6 + bacterium + light	100 (100)	6.25 (12.5)	6.25 (6.25)	6.25 (6.25)
M-0.6 + bacterium	400 (>800)	200 (400)	400 (400)	400 (>800)
Bacterium + light	>800 (>800)	>800 (>800)	>800 (>800)	>800 (>800)

20 mg in the composites resulted in higher MIC and MBC values. The results show that the use of a proper GO amount of 20 mg leads to the generation of the composite GO-20 with the best bactericidal performance, the presence of more GO in the composites may cause a drop in bactericidal performance due to its weaker bacterial inactivation compared with photo-induced antibacterial activity from TiO₂ and intrinsic antibacterial property from dissolved Ag⁺. Similar tendency in the bactericidal activity was observed for the composites prepared from different molar ratios of Ag₃PO₄/P25. The two-phase composite Ag₃PO₄/GO (M-0), in the absence of P25, exhibited a moderate bactericidal performance against all bacteria. With the increasing amount of P25 in the composite (from 1 to 0.6) the obtained three-phase composites showed enhanced bactericidal performance with lower MIC and MBC values against three typical pathogenic bacteria (*S. aureus*, *S. typhi* and *P. aeruginosa*). Composites (M-0.4, M-0.2) with lower Ag₃PO₄/P25 molar ratios exhibited decrease antibacterial property, implying that the molar ratio Ag₃PO₄/P25 plays a crucial role in determining bactericidal performance of the composites.

In order to further investigate the inactivation of bacteria over different materials, control experiments of bacterium alone, Ag₃PO₄, P25, the P25/Ag₃PO₄/GO composite M-0.6 with bacterium

under light irradiation, as well as M-0.6 with bacterium in dark were performed, MIC and MBC results are shown in Table 3. It is clearly shown that direct light irradiation has a negligible effect on the bacterial growth, while Ag₃PO₄ and P25 revealed a moderate inactivation of bacteria with a concentration ranging from 100 to 400 ppm. Although Ag₃PO₄ may demonstrate a good antibacterial activity, it is more likely to be reduced to metallic Ag by the light irradiation, resulting in the increase in MIC and MBC values. However, under light irradiation, the composite M-0.6 showed improved bactericidal activity toward all four pathogenic bacteria. The enhancement can be attributed to synergistic effect of intrinsic bactericidal activity of dissolved Ag⁺ and photo-induced bacterial killing of semiconductors P25 as well as Ag₃PO₄. The reduction of Ag⁺ to metallic Ag could be effectively avoided by the charge transfer of photo-generated electrons into the surfaces of P25 and GO. The absence of light caused an obvious deterioration in the bacterial killing of the M-0.6, indicating the light irradiation play an important role in obtaining better bactericidal performance of the composite M-0.6.

On the basis of MIC and MBC results, the P25/Ag₃PO₄/GO ternary composite M-0.6 was chosen for further investigation. For the purpose of investigating rapidity and duration, the effect of cultivation

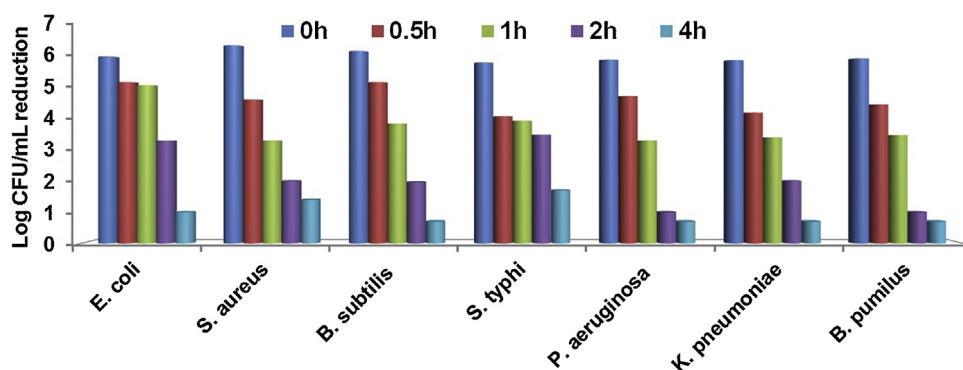


Fig. 9. Time-kill results of the P25/Ag₃PO₄/GO composite M-0.6 against bacteria.

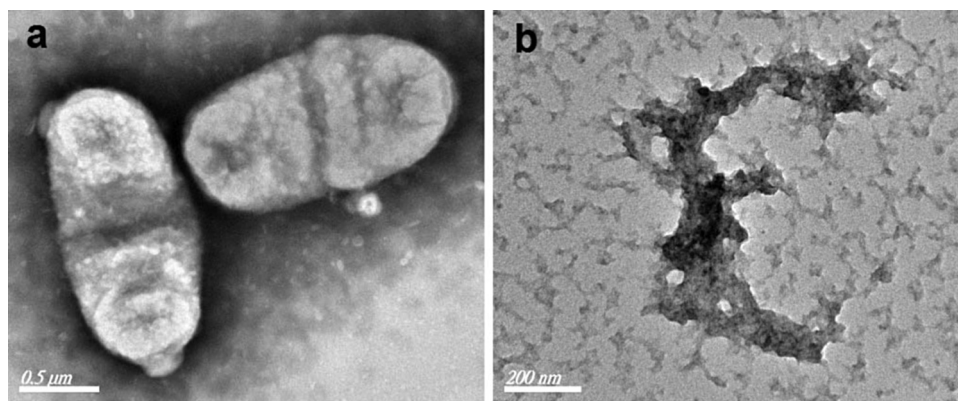


Fig. 10. TEM images of *E. coli* cells before (a) and after (b) the incubation with the P25/Ag₃PO₄/GO composite M-0.6.

time on the bactericidal efficiency has been assessed and the results of time-kill studies are presented in Fig. 9. It is shown that, when the cells were incubated for a period of 1 h, an obvious decrease was observed in the bacterial population from 6 to 6.5 Log CFU/mL of the control to 3–4 Log CFU/mL for most bacteria, indicating that a faster bactericidal rate of more than 99% can be achieved in 1 h. When the incubation period was prolonged to 4 h, bacterial counts continued to decrease and the majority of the bacterial population were found in 0.7–1.8 Log CFU/mL. Based on the MIC, MBC and time-kill results, it is concluded that the obtained composite demonstrates broad-spectrum bactericidal activity toward different kinds of pathogenic bacteria and it also presents relatively higher antibacterial rapidity and longer duration of killing.

Furthermore, the morphological changes of typical Gram-negative bacteria *E. coli* cells before and after the disinfection process were further analyzed by TEM characterization. As shown in Fig. 10a, in the absence of the P25/Ag₃PO₄/GO composite M-0.6, the original *E. coli* cells remained in a good state with a short rod-like structure, the diameter of single *E. coli* cell is 0.85–1 μm. However, when the composite was employed into *E. coli* cells and the mixture was incubated for 4 h, it is evident from Fig. 10b that *E. coli* cells were ruptured and the release of cytoplasm could be observed, regular short rod-like cellular shapes and bigger cell sizes disappeared. Such irreversible cellular damage proves the effectiveness of the bactericidal activity of the P25/Ag₃PO₄/GO composite M-0.6. It is generally accepted that antimicrobial materials interact with microbial cells through a variety of mechanisms. The major antimicrobial mechanisms indicate that the specific material can either directly interact with the microbial cells (interrupting transmembrane electron transfer, disrupting/penetrating the cell envelope,

oxidizing cell components) or produce secondary products (reactive oxygen species (ROS) or dissolved metal ions) that cause damage. In this study, excellent bactericidal performance of the P25/Ag₃PO₄/GO composite is attributed to ROS generated in the irradiated photocatalytic system, antibacterial Ag⁺ ions, as well as high-surface-area GO sheets.

On the basis of the above photocatalytic degradation and bactericidal results, it is suggested that the P25/Ag₃PO₄/GO composite have improved activities compared to P25, the bulk Ag₃PO₄ and also two-phase composites because of synergistic effect of irradiated P25 and Ag₃PO₄ on high-surface-area GO sheets. A schematic drawing illustrating the synergistic effect in the photocatalytic degradation of RhB and inactivation of bacteria over the P25/Ag₃PO₄/GO composite is shown in Fig. 11. The presence of high-surface-area GO sheets leads higher adsorption capacity of dye molecules and bacteria. Under visible light irradiation, Ag₃PO₄ can be irradiated and GO may also be transferred to reduced graphene oxide (RGO). The photogenerated electrons in the CB of Ag₃PO₄ move to the surface of reduced GO sheet that acts as a photo-induced electrons acceptor. On the one hand, the fast charge transfer from Ag₃PO₄ to reduced GO surface may keep electrons away from the bulk Ag₃PO₄, leading to the enhanced photostability of Ag₃PO₄. On the other hand, the absorbed oxygen on RGO/GO surface reacts with electrons to produce reactive oxygen species (ROS), mainly superoxide radicals (O₂^{•−}). The produced ROS can degrade dye molecules and also attack common pathogenic bacteria. Moreover, photoinduced holes in the VB of Ag₃PO₄ transfer to the VB of TiO₂, although it cannot be irradiated by the visible light (λ > 420 nm), the active holes can directly oxidize dye molecules and bacteria.

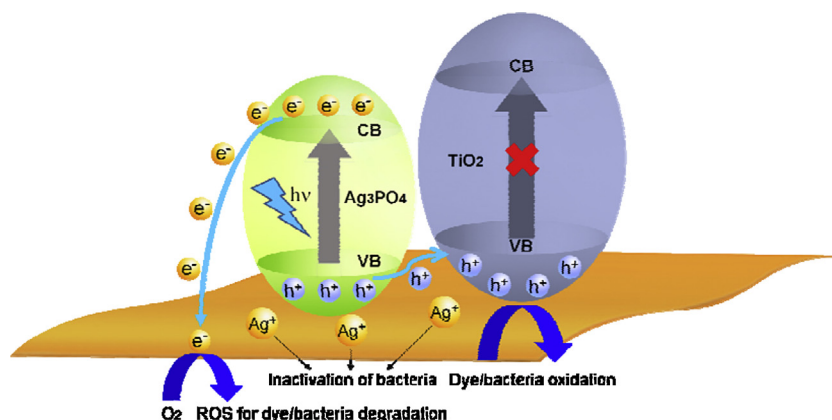


Fig. 11. A schematic illustration of the proposed mechanism for visible-light-driven photocatalytic degradation of RhB and inactivation of bacteria.

More photogenerated electrons and holes are produced via the pathway and continuously attack organic pollutant and bacteria in this way, efficiently suppressing the charge recombination and enhancing the photodegradation performance of organic pollutants and bacteria. It is also notable that also dissolved Ag^+ ions show inactivation of bacteria even in dark. However, its antibacterial activity may decrease under light irradiation due to the reduction of Ag^+ ions into metallic Ag. Thus it is proposed that the improved photocatalytic degradation of organic pollutants and bactericidal performance are attributed to synergistic effect of the photo-irradiated $\text{P25}/\text{Ag}_3\text{PO}_4/\text{GO}$ composite.

4. Conclusion

In summary, we report the facile synthesis of $\text{P25}/\text{Ag}_3\text{PO}_4/\text{GO}$ ternary composite photocatalysts by the electrostatically-driven assembly of Ag^+ on the few-layer GO surface, followed by the addition of P25 and the transformation of Ag^+ to Ag_3PO_4 . The ternary composites revealed a well-defined heterostructure where micro-sized Ag_3PO_4 particles and TiO_2 nanoparticles decorated on high-surface-area GO nanosheets. The obtained composites demonstrated enhanced solar light harvesting, improved solar photocatalytic degradation of RhB and excellent bactericidal performance. The reaction mechanism of the ternary composites was carefully studied by radicals capture experiments. Our results showed that photogenerated electrons in CB of Ag_3PO_4 move to the GO surface while holes left in VB of Ag_3PO_4 transfer to P25, suggesting that the recombination of electron-hole pairs could be effectively suppressed. Active holes and ROS produced under light illumination are considered to be responsible for highly efficient photocatalytic removal of RhB and pathogenic bacteria. We believe that this work opens the possibility to design new multifunctional composite materials for their application in photocatalytic elimination of pollutants in wastewater.

Acknowledgements

This work was financially supported by the National Natural Science Foundation of China (51102116, 51302112, 11102075), Natural Science Foundation of Jiangsu (BK2011480, BK2011534), Open Fund of Key Laboratory for Intelligent Nano Materials and Devices of the Ministry of Education (INMD-2014M02), and the Excellent Young Teachers Program of Jiangsu University, China. We thank Dr. Menny Shalom from Max Planck Institute of Colloids and Interfaces, Germany for helpful discussion and assistance in polishing the manuscript.

Appendix A. Supplementary data

Supplementary data associated with this article can be found, in the online version, at <http://dx.doi.org/10.1016/j.apcatb.2014.11.028>.

References

- [1] S. Kumar, W. Ahlawat, G. Bhanjana, S. Heydarifard, M.M. Nazhad, N. Dilbaghi, J. Nanosci. Nanotechnol. 14 (2014) 1838–1858.
- [2] A.B. Baranda, A. Barranco, I.M. de Marañon, Water Res. 46 (2012) 669–678.
- [3] A. Zapata, S. Malato, J.A. Sanchez-Perez, I. Oller, M.I. Maldonado, Catal. Today 151 (2010) 100–106.
- [4] S. Malato, P. Fernandez-Ibanez, M.I. Maldonado, J. Blanco, W. Gernjak, Catal. Today 147 (2009) 1–59.
- [5] T. Ahmed, S. Imdad, K. Yaldrum, N.M. Butt, A. Pervez, Desalin. Water Treat. 52 (2014) 4089–4101.
- [6] R.D. Ambashta, M. Sillanpää, J. Hazard. Mater. 180 (2010) 38–49.
- [7] D. Venieri, A. Fraggadakis, M. Kostadima, E. Chatzisympson, V. Binas, A. Zachopoulos, G. Kiriakidis, D. Mantzavinos, Appl. Catal. B: Environ. 154 (2014) 93–101.
- [8] L. Liu, H.W. Bai, J.C. Liu, D.D. Sun, J. Hazard. Mater. 261 (2013) 214–223.
- [9] W.J. Wang, L.Z. Zhang, T.C. An, G.Y. Li, H.Y. Yip, P.K. Wong, Appl. Catal. B: Environ. 108 (2011) 108–116.
- [10] M.D. Hernandez-Alonso, F. Fresno, S. Suarez, J.M. Coronado, Energy Environ. Sci. 2 (2009) 1231–1257.
- [11] Q.J. Xiang, J.G. Yu, M. Jaroniec, Chem. Soc. Rev. 41 (2012) 782–796.
- [12] H. Tong, S.X. Ouyang, Y.P. Bi, N. Umezawa, M. Oshikiri, J.H. Ye, Adv. Mater. 24 (2012) 229–251.
- [13] A. Kubacka, M. Fernandez-Garcia, G. Colon, Chem. Rev. 112 (2012) 1555–1614.
- [14] M.V. Sofianou, V. Psycharis, N. Boukos, T. Vaimakis, J.G. Yu, R. Dillert, D. Bahnemann, C. Trapalis, Appl. Catal. B: Environ. 142 (2013) 761–768.
- [15] K.L. Lv, B. Cheng, J.G. Yu, G. Liu, Phys. Chem. Chem. Phys. 14 (2012) 5349–5362.
- [16] S.W. Liu, J.G. Yu, M. Jaroniec, Chem. Mater. 23 (2011) 4085–4093.
- [17] K.L. Lv, Q.J. Xiang, J.G. Yu, Appl. Catal. B: Environ. 104 (2011) 275–281.
- [18] Q.J. Xiang, J.G. Yu, M. Jaroniec, Chem. Commun. 47 (2011) 4532–4534.
- [19] J.G. Yu, G.P. Dai, B. Cheng, J. Phys. Chem. C 114 (2010) 19378–19385.
- [20] S.W. Liu, J.G. Yu, M. Jaroniec, J. Am. Chem. Soc. 132 (2010) 11914–11916.
- [21] X.Y. Pan, M.Q. Yang, X.Z. Fu, N. Zhang, Y.J. Xu, Nanoscale 5 (2013) 3601–3614.
- [22] D.J. Martin, N. Umezawa, X.W. Chen, J.H. Ye, J.W. Tang, Energy Environ. Sci. 6 (2013) 3380–3386.
- [23] Z.B. Jiao, Y. Zhang, H.C. Yu, G.X. Lu, J.H. Ye, Y.P. Bi, Chem. Commun. 49 (2013) 636–638.
- [24] H.Y. Hu, Z.B. Jiao, H.C. Yu, G.X. Lu, J.H. Ye, Y.P. Bi, J. Mater. Chem. A 1 (2013) 2387–2390.
- [25] Y.P. Bi, H.Y. Hu, S.X. Ouyang, G.X. Lu, J.Y. Cao, J.H. Ye, Chem. Commun. 48 (2012) 3748–3750.
- [26] Y.P. Bi, H.Y. Hu, Z.B. Jiao, H.C. Yu, G.X. Lu, J.H. Ye, Phys. Chem. Chem. Phys. 14 (2012) 14486–14488.
- [27] Z.G. Yi, J.H. Ye, N. Kikugawa, T. Kako, S.X. Ouyang, H. Stuart-Williams, H. Yang, J.Y. Cao, W.J. Luo, Z.S. Li, Y. Liu, R.L. Withers, Nat. Mater. 9 (2010) 559–564.
- [28] Y. Bi, S. Ouyang, N. Umezawa, J. Cao, J. Ye, J. Am. Chem. Soc. 133 (2011) 6490–6492.
- [29] X.H. Yan, Q.X. Gao, J.L. Qin, X.F. Yang, Y. Li, H. Tang, Ceram. Int. 39 (2013) 9715–9720.
- [30] X.F. Yang, H.Y. Cui, Y. Li, J.L. Qin, R.X. Zhang, H. Tang, ACS Catal. 3 (2013) 363–369.
- [31] P.Y. Dong, Y.H. Wang, B.C. Cao, S.Y. Xin, L.N. Guo, J. Zhang, F.H. Li, Appl. Catal. B: Environ. 132 (2013) 45–53.
- [32] J.J. Guo, S.X. Ouyang, P. Li, Y.J. Zhang, T. Kako, J.H. Ye, Appl. Catal. B: Environ. 134 (2013) 286–292.
- [33] Y.P. Liu, L. Fang, H.D. Lu, Y.W. Li, C.Z. Hu, H.G. Yu, Appl. Catal. B: Environ. 115 (2012) 245–252.
- [34] L. Liu, J.C. Liu, D.D. Sun, Catal. Sci. Technol. 2 (2012) 2525–2532.
- [35] H.Y. Cui, X.F. Yang, Q.X. Gao, H. Liu, Y. Li, H. Tang, R.X. Zhang, J.L. Qin, X.H. Yan, Mater. Lett. 93 (2013) 28–31.
- [36] X.F. Yang, J.L. Qin, Y. Jiang, R. Li, Y. Li, H. Tang, RSC Adv. 4 (2014) 18627–18636.
- [37] X.J. Zhou, J.L. Qiao, L. Yang, J.J. Zhang, Adv. Energy Mater. 4 (2014) 1301523.
- [38] V. Chabot, D. Higgins, A.P. Yu, X.C. Xiao, Z.W. Chen, J.J. Zhang, Energy Environ. Sci. 7 (2014) 1564–1596.
- [39] Y.W. Zhu, S. Murali, W.W. Cai, X.S. Li, J.W. Suk, J.R. Potts, R.S. Ruoff, Adv. Mater. 22 (2010) 3906–3924.
- [40] F. Kim, L.J. Cote, J.X. Huang, Adv. Mater. 22 (2010) 1954–1958.
- [41] N. Zhang, Y.H. Zhang, X.Y. Pan, M.Q. Yang, Y.J. Xu, J. Phys. Chem. C 116 (2012) 18023–18031.
- [42] N. Zhang, S.Q. Liu, X.Z. Fu, Y.J. Xu, J. Phys. Chem. C 115 (2011) 9136–9145.
- [43] Y.H. Zhang, Z.R. Tang, X.Z. Fu, Y.J. Xu, Appl. Catal. B: Environ. 106 (2011) 445–452.
- [44] Y.H. Zhang, Z.R. Tang, X.Z. Fu, Y.J. Xu, ACS Nano 4 (2010) 7303–7314.
- [45] Y.H. Zhang, Z.R. Tang, X. Fu, Y.J. Xu, ACS Nano 5 (2011) 7426–7435.
- [46] S.Q. Liu, N. Zhang, Z.R. Tang, Y.J. Xu, ACS Appl. Mater. Interfaces 4 (2012) 6378–6385.
- [47] Z. Chen, Y.J. Xu, ACS Appl. Mater. Interfaces 5 (2013) 13353–13363.
- [48] X.F. Yang, J.L. Qin, Y. Li, R.X. Zhang, H. Tang, J. Hazard. Mater. 261 (2013) 342–350.
- [49] H. Tang, D. Zhang, G.G. Tang, X.R. Ji, W.J. Li, C.S. Li, X.F. Yang, Ceram. Int. 39 (2013) 8633–8640.
- [50] D.C. Marcano, D.V. Kosynkin, J.M. Berlin, A. Sinitskii, Z.Z. Sun, A. Slesarev, L.B. Alemany, W. Lu, J.M. Tour, ACS Nano 4 (2010) 4806–4814.